Formation of (Rh−Fe)−FeO_x Complex Sites Enables Methanol Synthesis from CO_2

Yifeng Zhu,[▽] Ran Luo,[▽] Honghong Shi, Katherine Koh, Libor Kovarik, John L. Fulton, Johannes A. Lercher, Zhi-Jian Zhao,* Jinlong Gong,* and Oliver Y. Gutiérrez*

ABSTRACT: We addressed the challenges of designing catalysts for selective CO_2 hydrogenation by incorporating Fe oxide species onto Rh nanoparticles. Nanoscopic FeO_x domains created a "reverse catalyst" structure (i.e., a metal oxide supported on a metal) that increased the density of interfacial sites compared to traditional supported catalysts. The contact between the metal nanoparticle and the oxide overlayer induced the formation of a surface Rh−Fe alloy that stabilized methoxy groups while suppressing hydrogenolysis to methane. Sites at FeO_x−metal interfaces interact with CO_2 much stronger than sites on metal surfaces, show larger energy barriers to cleave the C−O bonds, and offer a barrierless pathway for the hydrogenation of methoxy species to methanol. Consequently, the multifunctional sites over FeO_x/Rh−Fe catalysts highlight and meet the requirements of a selective methanol catalyst: strong interaction with CO_2 to ensure a high density of transition states, metal sites to activate and make hydrogen available to surface intermediates, and high energy barriers for C−O bond cleavage to form carbides. These synthetic and catalytic chemistries, demonstrated for Rh−Fe−FeO_x interfaces, enable us to overcome the limitations to the design of methanol production catalysts.

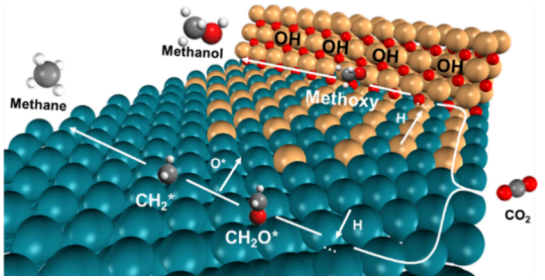

KEYWORDS: *CO_2 conversion, methanol synthesis, heterogeneous catalysis, multifunctional catalyst, bimetallic catalysts*

INTRODUCTION

Methanol synthesis is an attractive alternative for using and upgrading CO_2, particularly when integrated with a subsequent step to produce energy carriers and bulk chemicals (i.e., methanol-to-gasoline and methanol-to-olefins).[1−3] Platinum-group metals are excellent hydrogenation catalysts, but they typically show low rates of CO_2 hydrogenation and produce methane and light hydrocarbons as main products.[4] This is because CO_2 barely adsorbs on the surfaces of such metals, but once adsorbed it is readily dissociated to oxygenated intermediates (e.g., CO).[5−7] Then, the second C−O bond is cleaved, and the resulting surface carbide is hydrogenated into methane or hydrocarbons upon metal-catalyzed C−C coupling.[8] Suppression of the metal surfaces, either by covering them with metal oxide adlayers[9] or by decreasing the dimension of the metal particles to subnanometer clusters and single metal cations,[10,11] hinders complete C−O bond cleavage. This effectively shifts the selectivity from hydrocarbons to CO.[10,11] Promoters such as Li, Ti, Mn, Fe, and Co improve the selectivity of metals to oxygenated compounds, but these promoting effects are difficult to control and usually lead to wide product distributions, with CO and methane still being major products.[12−15] Efficient conversion of CO_2 to methanol requires both strong adsorption of CO_2 and fast hydrogenation of surface intermediates while preserving one C−O bond.[16,17] These requirements are met at active sites located at interfaces between metals and metal oxides. The associated challenge for catalyst design is to maximize the density of interfaces either by stabilizing tiny metal particles or by placing metal particles within three-dimensional frameworks.[11,18,19]

Another route toward the design of novel catalysts for methanol production would be to tune the nature of metal−metal oxide interfaces, making them intrinsically more active. Unfortunately, there are only a few combinations of metals and metal oxides that have been proven efficient in the reaction, mainly Cu and Pd combined with ZnO or ZrO_2.[4,16] The challenge remains as to how to increase the intrinsic activity for hydrogen addition while avoiding the usual trade-off of losing selectivity to methanol. Consequently, designing catalytic sites that meet the requirements to activate CO_2 and selectively hydrogenate the intermediates toward methanol using a wide variety of transition metals remains a forefront topic.

The goal of our work was to use a novel approach to address both challenges for the design of catalysts for selective CO_2

hydrogenation (i.e., enhancing the density of metal−metal oxide interfaces and their intrinsic activity). We deposited nanoscopic FeO_x oxide domains on the surface of Rh nanoparticles while inducing the formation of surface Rh−Fe alloys, taking advantage of the atomic contact of Rh particles with FeO_x overlayers. We found that the mixed metal phase stabilizes methoxy groups while suppressing hydrogenolysis to methane. This property complements the strong interaction with CO_2 that the FeO_x nanostructures give to the inverse catalysts, thereby allowing the production of methanol at high rates (Figure 1). Thus, the key for the performance of the

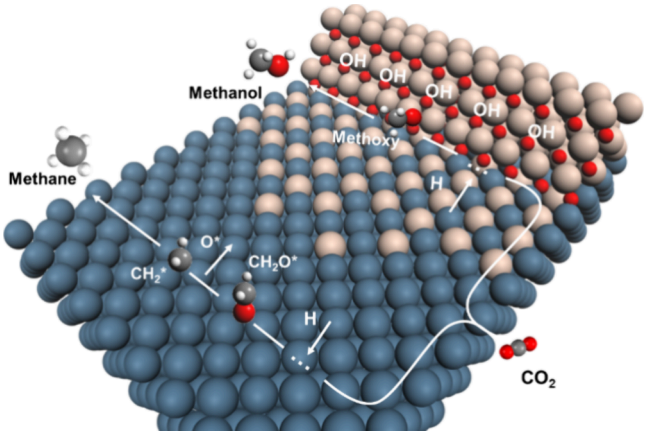

Figure 1. Schematic representation of routes for CO_2 hydrogenation on a Rh surface and an alloyed Rh−Fe surface with FeO_x adlayers. The pure metallic surface leads to methane production, while the interface yields methanol.

catalyst is the proximity of the surface Rh−Fe alloy to the sites at the FeO_x overlayer. The resulting synergy produced a catalyst that provides outstanding performance compared with other systems reported in the literature (Supplementary Note 1). Also, we show how the design of complex catalytic sites turns unselective metals into selective methanol catalysts with enhanced rates for CO_2 conversion.

RESULTS AND DISCUSSION

Effect of FeO_x Overlayers on the Performance of Rh. We covered Rh nanoparticles with FeO_x adlayers by immersing preformed Rh nanoparticles (2−3 nm, Figure S1) in solutions with varying concentrations of Fe^{2+} ions. These cations adsorb on metals in aqueous media, leading to nanoparticles decorated with FeO_x overlayers (Fe^{3+} cations do not adsorb at the same conditions).[19] The size of the FeO_x domains depends on the concentration of Fe^{2+} precursors in solution. Thus, the FeO_x-modified Rh nanoparticles prepared for this study are denoted in the following as Rh−xFe/SiO_2, where x indicates the Fe/Rh molar ratio used in the synthesis. The Fe/Rh molar ratios of the resulting materials, dispersed in SiO_2 for handling, increased to ∼1.6 as the concentration of Fe^{2+} in solution increased (Figure S2).

These Rh−xFe/SiO_2 materials were active for the hydrogenation of CO_2 to methanol (Figure 1). In contrast, the parent Rh nanoparticles dispersed in SiO_2 (denoted as Rh/SiO_2) only produced methane in the temperature range tested (150−260 °C), which agrees with previous reports.[12] Figure 2b shows that the methanol production rate at 32 bar increased from 0 mol mol_{Rh}^{-1} h^{-1} on Rh/SiO_2 to 4−10 mol mol_{Rh}^{-1} h^{-1} on Rh−2Fe/SiO_2 (which had a Fe/Rh molar ratio of ∼1.4)

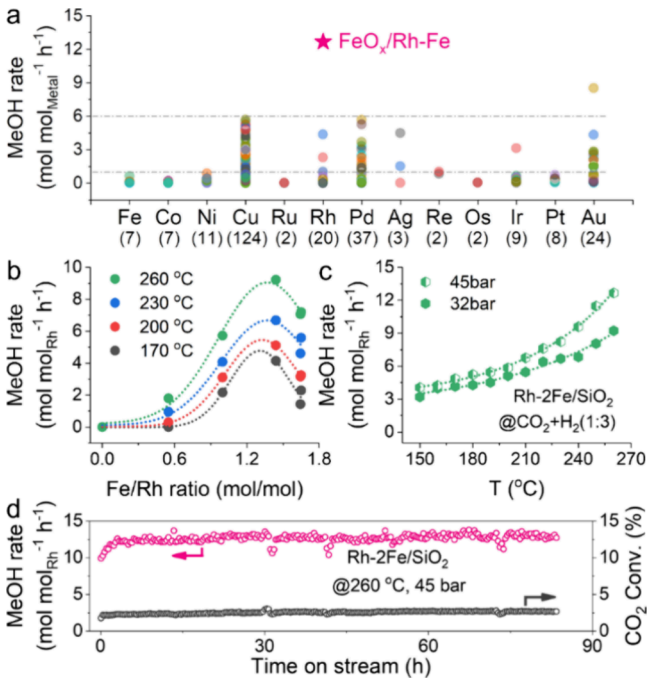

Figure 2. Graphical survey comparing the rates of methanol (MeOH) production using catalysts reported in the literature with the performance of a catalyst reported in this work (FeO_x/Rh−Fe). (a) The numbers under the metal symbols represent the number of examples found in our survey. (b) Rates of MeOH production from CO_2 hydrogenation (32 bar) as a function of the Fe/Rh molar ratios of the catalysts. (c) Rates observed using Rh−2Fe/SiO_2 at varying pressures. (d) Stability test at under 260 °C and 45 bar.

and then decreased for materials with higher Fe/Rh ratios. The rates of methanol formation and the corresponding conversions of CO_2 and selectivity to methanol are tabulated in Tables S1−S3. The changes of methanol production rates and selectivity with temperature are shown in Figure S3. The Rh−2Fe/SiO_2 catalyst exhibited the highest methanol production rate of 9.2 mol_{Rh}^{-1} h^{-1} at 260 °C and 32 bar. This rate increased further to 12.7 mol_{Rh}^{-1} h^{-1} when the pressure was increased to 45 bar (Figure 2c). The selectivity to methane can be suppressed to less than 20% while the methanol selectivity can be 50−80% at temperatures lower than 200 °C (Figure S4). Moreover, the catalyst was stable and showed a constant methanol rate for over 80 h (Figure 2d).

Characterization of the Catalyst Structure. The structure of the sample that showed the highest methanol yield (Rh−2Fe/SiO_2) was characterized by XAS for average structural information regarding the Rh and Fe coordination environment and valence state (Supplementary Notes 2 and 3). We found clear evidence of Fe phase segregation, supporting the structure suggested from the STEM results. The X-ray absorption near edge structure (XANES) of this sample revealed features of mixed Fe^0 and Fe^{3+} species (Figure S18). From the extended X-ray absorption fine structure (EXAFS; Table S5 and Figure S13), oxygen was found as the nearest neighbor of Fe with a bond length of 1.81 Å, whereas the bonding of Fe−Rh at 2.58 Å (CN_{Fe-Rh} = 2.1 ± 0.4) and further distances of the bimetallic Rh−Fe structures (4.33 and 4.92 Å) were also observed in the fitting of the Fe K edge spectra. In addition, we have performed a careful analysis to distinguish the mentioned direct Fe−Rh bond from the possible Fe−Fe bond at the interface of iron oxide and Rh

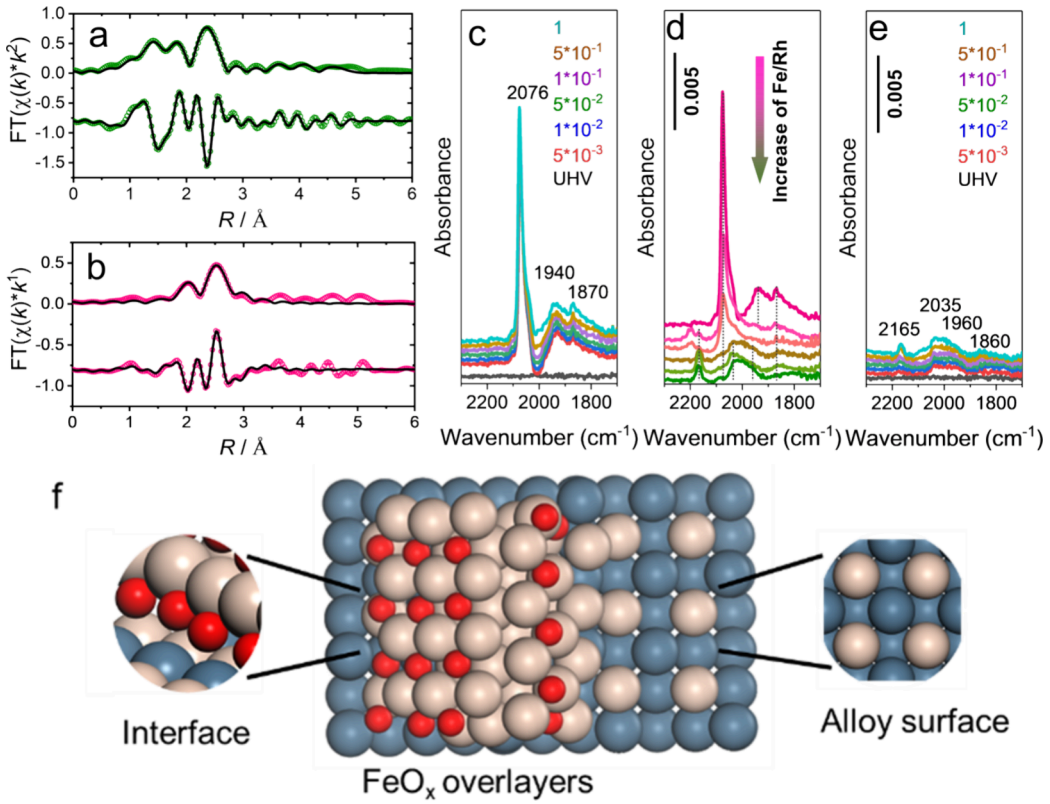

Figure 3. (a) Fe K edge and (b) Rh K edge EXAFS spectra of Rh−2Fe/SiO_2. Infrared spectra of CO adsorbed on (c) Rh−2Fe/SiO_2, (d) Rh/SiO_2, and (e) Rh−*x*Fe/SiO_2 with different Fe/Rh ratios. (f) Optimized structural model for (Rh−Fe)−FeO_x and its main features: FeO_x overlayers, surface alloy, and an oxide−alloy interface. The Malta blue, light yellow, and red spheres depict Rh, Fe, and O atoms, respectively.

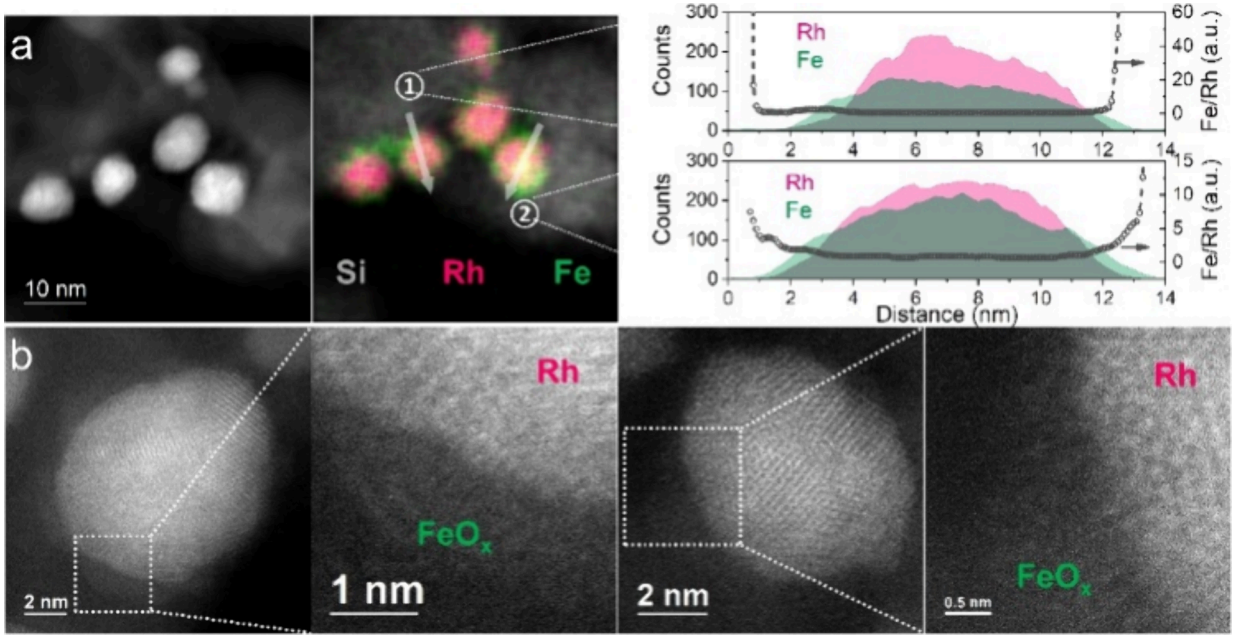

Figure 4. (a) High-angle angular dark-field scanning transmission electron microscopy (HAADF-STEM) image coupled with X-ray energy-dispersive microscopy mapping and line-scan profile analysis. (b) High resolution HAADF-STEM image of Rh−2Fe/SiO_2 revealing the presence of an FeO_x overlayer on the metal surface.

nanoparticles (Supplementary Notes 2 and 3). Due to the high temperature of the H_2 treatment (400 °C), it is reasonable that a fraction of Fe at the interface of the oxide shell on Rh nanoparticles is reduced to create the bimetallic Rh−Fe interface.

We observed that there is a very weak signal due to Rh−Fe coordination at 2.58 Å in the Rh K edge spectra of this sample (Figures S14 and S15 and Table s6). The fitting of the Fe K edge spectra provided a small but significant coordination number (CN_{Rh-Fe} = 0.7). This deviates from the bulk

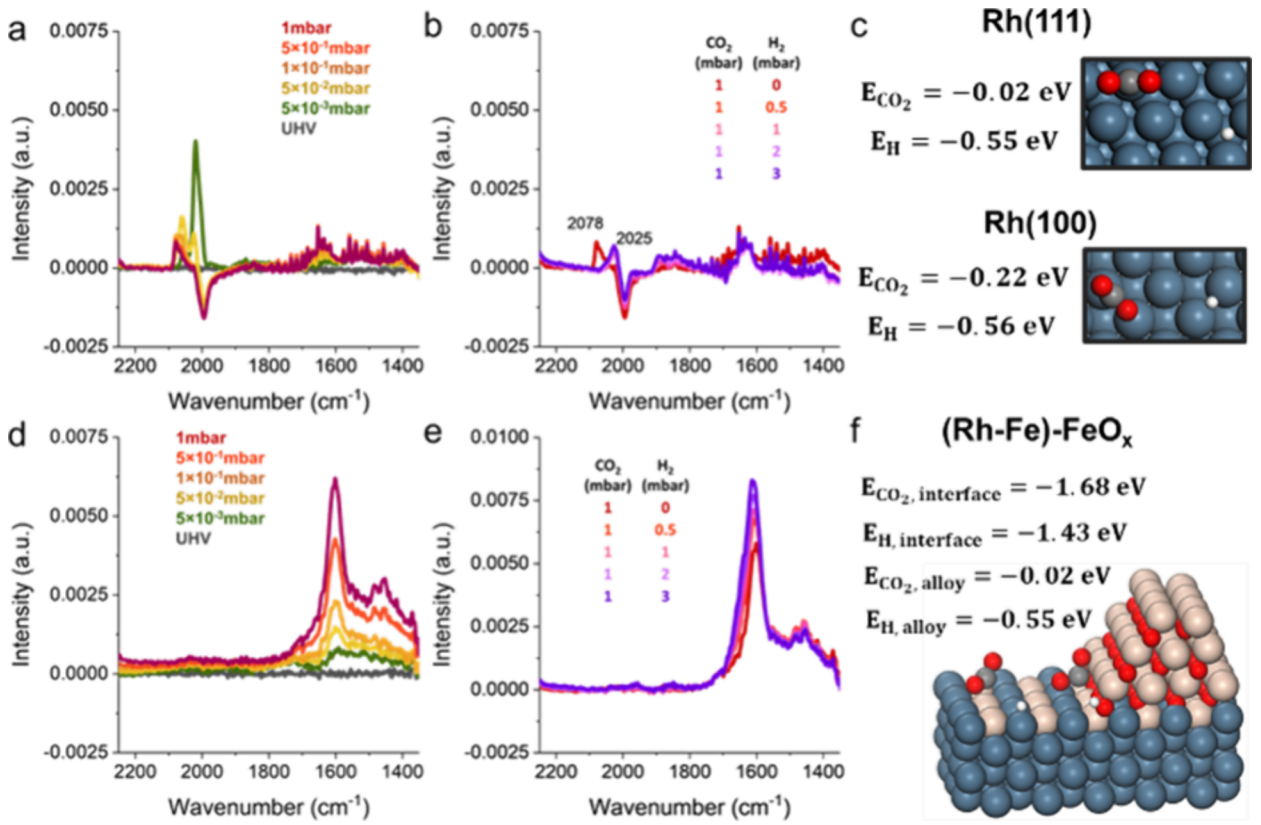

Figure 5. (a) Infrared spectra of CO_2 adsorbed on Rh/SiO_2. (b) IR spectra illustrating the effect of H_2 on CO_2 adsorption (coadsorption) on Rh/SiO_2. (c) Calculated adsorption energies of CO_2 and H_2 on Rh(111) and Rh(100). (d) IR spectra of CO_2 adsorbed on $Rh-2Fe/SiO_2$. (e) IR spectra illustrating the effect of H_2 on CO_2 adsorption (coadsorption) on $Rh-2Fe/SiO_2$. (f) Scheme for CO_2 and H_2 adsorption on metallic Rh−Fe and Rh−Fe−FeO_x (as concluded from the IR experiments) and calculated adsorption energies of corresponding species.

composition derived from ICP analysis, i.e., Fe and Rh loadings are comparable: 5.9×10^{-5} and 3.8×10^{-5} mol/g_{cata}, respectively, in the $Rh-2Fe/SiO_2$ sample. This is easily explained by the clear phase segregation of Fe. That is, not all of the Fe atoms bond with Rh. Furthermore, the Rh particle size is about 5 nm, which makes the proportion of the surface Rh atoms small compared to those in the bulk. Hence, the results from the EXAFS of the Rh K edge suggest that the bimetallic Fe−Rh species locates at the interface of Rh nanoparticle with the iron oxide layer rather than homogeneously through the whole Rh particle.

We performed a CO adsorption analysis using infrared spectroscopy (IR) to further characterize the structure of the active phase (Figure 3c−e). Bands of CO adsorbed on Rh/SiO_2 appeared at 2075, 1940, and 1870 cm^{-1}, which correspond to CO adsorbed in linear (Rh−CO), bridging (Rh_2−CO), and hollow modes (Rh_3−CO), respectively (Figure 3c). Carbon monoxide saturates the surface of Rh in Rh/SiO_2 at pressures as low as 5×10^{-3} mbar (Figure S5a). As the Fe content increased in the Rh−Fe catalysts, the bands of linearly adsorbed and bridging CO shifted toward lower wavenumbers and decreased in intensity (Figures 3d and S5). Both effects are related to the electronic interactions between Fe species and metallic Rh and to the decreased number of exposed metal sites. For $Rh-2Fe/SiO_2$, we attributed the broad band at 2035 cm^{-1} to CO adsorbed linearly on Fe−Rh alloyed sites, while bands at 1960 and 1860 cm^{-1} are attributed to bridging CO (Figure 3e). We also observed bands at 2150−2170 cm^{-1}, which were attributed to CO species adsorbed on Fe^{2+} cations. Hence, the model proposed for the Rh−xFe/SiO_2 catalyst series includes Rh nanoparticles with Fe atoms incorporated in the outer layers (surface alloy) and partially covered by FeO_x domains (Figure 3f).

We performed a microscopy analysis of $Rh-2Fe/SiO_2$ to support the model derived from EXAFS and CO-IR spectroscopy. Typical images and line-profile scans (Figure 4a) showed that Fe species are distributed on the surfaces of Rh nanoparticles. The high-resolution images in Figure 4b show an FeO_x layer with low contrast and thickness of a few angstroms on the Rh nanoparticles. We also performed in situ high-resolution transmission electron microscopy imaging of the catalyst after reduction at 400 °C in H_2 to avoid the possibility of the catalyst changing during handling. The analysis also showed the presence of an amorphous FeO_x overlayer on the metal surface (Figure S6). Note that the average particle sizes of $Rh-2Fe/SiO_2$ and Rh/SiO_2 are both ∼5 nm with similar particle size distributions. These average particle sizes did not change after being exposed to the reaction conditions (Figure S7). Therefore, the differences in the catalytic performance are unrelated to differences in particle sizes.

We optimized a precise structural model based on the characterization results through density functional theory (DFT). For the surface alloy, we considered different possible arrangements of Fe on the Rh(100) and Rh(111) surfaces. Our DFT-optimized structures indicated that a Rh(100) surface with equimolar concentrations of Rh and Fe matches well both Fe−Rh and Rh−Rh bond lengths derived from the EXAFS fitting (Figure S20). A stability calculation shows that Fe tends to stay on the surface rather than in deeper layers (Table s8).

Then, a three layered (~0.8 nm) FeO overlayer, which is a stable structure compared with other candidates (Figure S21), was constructed on the surface alloy. Figure 3f shows the final atomic model, which contains the alloy surface and the alloy−oxide interface as key synergistic sites.

Insights into Adsorption and Activation. We performed CO_2 adsorption and CO_2−H_2 coadsorption monitored by IR spectroscopy to understand the interactions of different surfaces with CO_2 (Figure 5). The full spectra are shown in Figures S8 and S9. Peaks in the 2300−2500 cm^{-1} range are attributed to gas-phase CO_2, peaks in the 1900−2200 cm^{-1} range are the result of adsorbed CO, and the peaks in the 1300−1800 cm^{-1} range correspond to (bi)carbonates. Spectra within the 1200−2400 cm^{-1} range are shown in Figure 5. On bare Rh metal surfaces of Rh/SiO_2, CO_2 dissociates to form adsorbed carbonyls (2020 cm^{-1}) at 5×10^{-3} mbar (Figure 5a). The carbonyl signal reached its maximum intensity at 5×10^{-3} mbar CO_2 and decreased at higher CO_2 pressures, while new signals appeared at higher wavenumbers of 2060 and 2080 cm^{-1}. The new signals are attributed to carbonyl species adsorbed on oxidized Rh cations bonding the oxygen dissociated from CO_2.[20,21] In addition, small amounts of surface carbonates were formed as the CO_2 pressure increased.

In the coadsorption experiments, while having 1 mbar CO_2 in the cell, we introduced 0.5−3 mbar H_2. Coadsorbing hydrogen shifted the carbonyl vibration from 2080 cm^{-1} back to 2020 cm^{-1} on Rh/SiO_2, indicating that Rh was reduced in the presence of H_2 (Figure 5b). However, the intensity of the CO vibration did not increase, which indicates that the reduction of Rh did not parallel any additional adsorption of CO/CO_2 from the gas phase (Figure S10a). This could be caused by partial blocking of the Rh surface by hydrogen species. Under the reaction conditions, the carbonyl species react with hydrides to form methane, wherein C−O dissociation is the rate-limiting step.[22]

The adsorption of CO_2 on $Rh-2Fe/SiO_2$, a material with a surface Rh−Fe alloy near Rh−O−Fe sites at the interface with the FeO_x overlayer, is significantly different from that on Rh/SiO_2. Figure 5d shows the absence of vibrations of adsorbed carbonyls upon dosing the material with CO_2 up to 1 mbar, suggesting that CO_2 does not readily dissociate under these conditions. The inability of the metal surface to dissociate CO_2 is attributed to the formation of the Rh−Fe alloy. In contrast, intense signals of carbonates appeared in the 1350−1750 cm^{-1} range, showing a Langmuir-type trend with the pressure of CO_2 (Figure S11). The apparent concentration of carbonates on $Rh-2Fe/SiO_2$ is higher than that on Rh/SiO_2. The much larger capacity of $Rh-2Fe/SiO_2$ than that of Rh/SiO_2 to adsorb CO_2 was corroborated by the temperature-programmed desorption of H_2 after CO_2 adsorption (Figure S12). The carbonate signals did not appreciably change as we dosed 0.5−3 mbar H_2 into the IR cell (Figures 3e and S10b). This suggests that H_2 did not adsorb on the same sites as did CO_2. Thus, we consider that carbonates are formed on the FeO_x overlayers or interfaces, while adsorbed hydrogen remains at metallic sites.

In the following discussion, we analyze the adsorption phenomena from a theoretical perspective using the model of the active site presented above (Figure 3f). The adsorption strengths of reactants on bare Rh surfaces as well as on the FeO_x and Rh−Fe alloyed sites offered by our $Rh-2Fe/SiO_2$ catalysts are key to their activation and subsequent reactions. Figure 5c and f shows the calculated adsorption energies of the main species involved in the reaction, which are in good agreement with the trends derived from the isotherm experiments. That is, weak CO_2 adsorption on Rh (−0.22 eV) limits the amount of adsorbed CO_2 species and therefore the rate of the subsequent reaction on pure Rh surfaces. At the metal−oxide interface, in contrast, the adsorption energy of CO_2 changes to −1.68 eV. In this region, carbon and one oxygen from CO_2 bind an oxygen and an Fe cation in the iron oxide cluster. The second oxygen of CO_2 binds to the metal surface to form a carbonate that bridges the iron oxide cluster and the alloy (Figure S22). The strong adsorption of this intermediate increases the abundance of transition states and, therefore, the rate of reaction.

Carbon monoxide is likely a key intermediate product during the conversion of CO_2. Thus, we analyzed its interaction with the catalysts. We used the variations of the integrated areas of IR bands of adsorbed CO to calculate adsorption constants according to the Langmuir−Hinshelwood formalism (Supplementary Note 4). The constants indicate that CO adsorbs more weakly on the Rh−Fe sites than on metallic Rh of Rh/SiO_2 (Figure S19 and Table S7). Our atomic simulation captured this behavior and showed the effects of coverage on the relative strength of adsorption of CO on Rh−Fe and metallic Rh sites. At low coverage, the adsorption strength of CO on Rh sites at the Rh−Fe alloyed surface is like that on Rh sites on the pure Rh surface (Figures S23 and S24). However, when the coverage of CO is larger than half a monolayer, Fe sites in the Rh−Fe surface participate in the binding, resulting in markedly weakened adsorption. According to the theoretical surface phase diagram (Figure S25), the CO coverage over the Rh−Fe surface is well above half a monolayer at the conditions of the IR measurements (from 5×10^{-3} to 1 mbar CO). Additionally, the theoretical position of the IR vibration band of CO adsorbed on Rh−Fe sites at high coverages was obtained (Figure S26), lying around 2035 cm^{-1}, in excellent agreement with the assignment of the experimental data (Figure 3). Thus, the theoretical results agree well with the weaker CO adsorption on $Rh-2Fe/SiO_2$ than on Rh/SiO_2 as concluded from the analysis of the CO-IR spectra.

The binding strength of CO on Fe^{2+} is even weaker than that on the Rh−Fe surface alloy, as the adsorption constant, determined from the Langmuir−Hinshelwood treatment of the IR spectra, is 5−8 times lower than that on Rh−Fe sites. This finding also was captured by our theoretical calculations, which indicated a weaker CO adsorption at the interfaces between metal and oxide clusters than on the metallic surface (Rh and Rh−Fe alloys) (i.e., the adsorption energy is −1.70 eV at the interface but −2.14 eV on metallic Rh.

We have shown that the adsorption of CO_2 is weak on metallic Rh,[11] while results from the IR experiments discussed above show that Rh readily dissociates CO_2 to surface carbonyl. This finding confirms previous conclusions from theoretical studies that CO_2 can barely adsorb on metallic Rh, whereas it can be dissociated by highly active open surfaces to O-containing intermediates (e.g., CO).[5−7,23] The second C−O bond is cleaved, and the carbon is hydrogenated into methane or hydrocarbons with low probability for the stabilization of the surface methanol precursors.[8] Therefore, Rh mainly produces methane with low CO_2 conversion rates. A markedly different scenario arises from the experiments described above for the $Rh-2Fe/SiO_2$ system. Here, the preferential sites for CO_2 activation are the interfacial sites of the FeO_x domains

formed on top of the metallic particle, while the Rh−Fe alloy does not dissociate CO_2 and interacts relatively weakly with CO under the IR study conditions.

Mechanistic Insights. We previously discussed how the modification of Rh nanoparticles with iron oxide overlayers enhances the yields and rates of methanol formation, thus completely changing the catalytic functionality of the initial metal. In the following discussion, we assess the possible intermediates and describe an analysis of the reaction pathways that involved combining theoretical calculations and in situ IR spectroscopy.

We monitored, by in situ IR spectroscopy (Figure 6), the conversion of CO_2 on Rh−2Fe/SiO_2 (1−24 bar in a mixture of

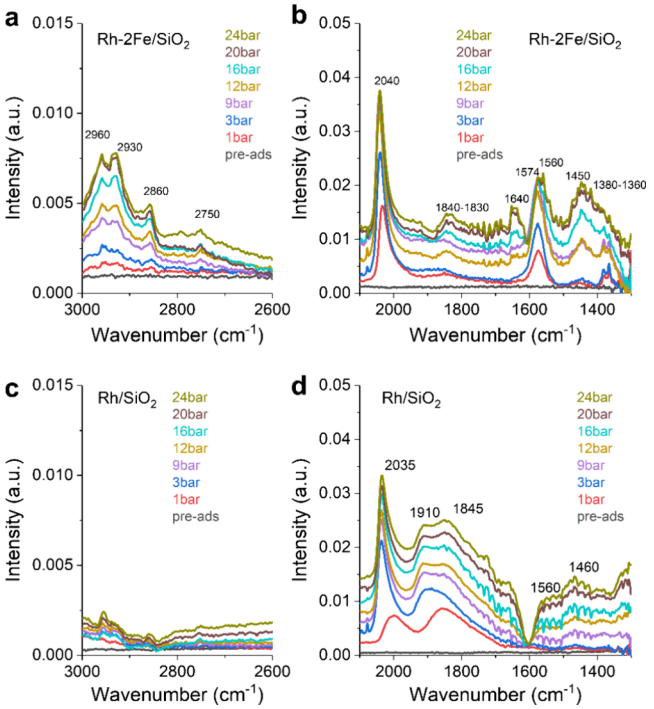

Figure 6. (a and b) In situ IR study at 200 °C and 1−24 bar of CO_2 + H_2 flow (CO_2/H_2 = 1:3) on Rh−2Fe/SiO_2, revealing the formation of a methoxy group and carbonyl and carbonate species on the surface. (c and d) In situ IR spectra of Rh/SiO_2 at 200 °C and 1−24 bar of CO_2 + H_2 flow (CO_2/H_2 = 1:3)

CO_2 and H_2 at 200 °C). The study showed different intermediates that agreed well with the theoretical analysis described above. We observed bands at 2750, 2860, 2930, and 2960 cm^{-1}, as well as in the range of 3000−2600 cm^{-1}. The 2750 cm^{-1} band corresponds to the vibration of formate, while the 2860−2960 and 1450 cm^{-1} bands belong to surface methoxy species (Figure 6a).[24,25] The intensities of these bands increased with the increase in pressure, in line with the higher productivity of methanol observed at increasing pressure (Figure 2c). Note that the analysis of the region below 1500 cm^{-1}, where more bands of methoxy species are expected, was hindered by an intense band of SiO_2. We also identified linearly adsorbed CO (2040 cm^{-1}), bridging CO (1840 cm^{-1}), bidentate carbonate (1574 and 1380−1360 cm^{-1}), and bicarbonate (1640 cm^{-1}) in the 2200−1300 cm^{-1} range.[26] Adsorbed CO, bidentate species, and a small amount of bicarbonate species were formed at 1−3 bar. The bands of bridging CO and bicarbonate species became more intense with an increasing reaction pressure. Calculated vibration frequencies of absorbed methoxy are shown in Table S9. Frequencies for C−H stretching have been overestimated by 30 cm^{-1}, which is normal in calculations for the anharmonic vibration of C−H stretching.[27]

On Rh/SiO_2, bands at 2035 cm^{-1} and in the 1910−1845 cm^{-1} range indicate a distribution of CO species, including on-top and bridging configurations (Rh−CO, Rh_2−CO, and Rh_3−CO). This wide distribution is expected on the extended Rh surface, in contrast to an Rh−Fe surface alloy that would not favor bridging and hollow adsorption configurations. Frequencies calculated for CO-Rh bands, shown in Table S10, are in good accordance with experimental values. Our calculated frequencies also indicate that the linear adsorption band mainly comes from CO on Rh(111). It worth emphasizing the appearance of the bands at 2860−2960 cm^{-1} in the IR spectra. These bands indicate the formation of methoxy species on Rh/SiO_2, albeit with a much lower intensity (coverage) than those on (Rh−Fe)−FeO_x. This can be associated with the low barriers toward surface carbides calculated on Rh (Figure 6a), and the finding agrees well with the lack of methanol detected in temperature-programmed desorption experiments and as a product during the reaction.

We started our theoretical analysis with adsorbed CO because it is the smallest surface oxygenated intermediate that can be used as a methanol precursor. Based on reported reaction networks for the conversion of CO* on Rh,[28] we calculated the barriers of possible pathways and intermediates on Rh(100) and Rh(111) as shown in Figure 7a and Figure S23. We found that the pathway from CO* to CH_2* (via CHO* and CH_2O*) on Rh(100) is the lowest-energy route toward a surface carbide, which would be readily hydrogenated to methane. In this route, CH_2O* is the key intermediate, as it is easier to dissociate its C−O bond rather than to add more hydrogen. In contrast, the Rh(111) surface seems to favor the formation of methoxy species (immediate methanol precursors) over carbide formation. However, the reactivity of this pathway is limited by weaker CO_2 adsorption (Figure 5c and f) and higher reaction barriers compare to the C−O bond cleavage route favored on Rh(100) (Figure 7b).

We also studied the barrier for the dissociation of the C−O bond of CHOH* on (Rh−Fe)−FeO_x, an easy step on metallic Rh (Figure 7a and Figures S27 and S28) to emphasize the differences between both active sites. As shown in Figure S29, on the metal-oxide interface, the CHOH* dissociation barrier is higher than that on metallic Rh surfaces, which explains the suppression of methanation.

Transitioning to the analysis of the last hydrogenation step on (Rh−Fe)−FeO_x, we first emphasize the important role of hydroxyl groups. We found experimentally that Rh−2Fe/SiO_2 has a higher concentration of −OH groups than Rh/SiO_2 under a H_2 atmosphere at 200 °C (Figure 7c). Hydroxyl groups influence the interaction strength of Rh−O−Fe sites with CO and CO_2[11] and may act as promoters that influence the stability of methoxy groups during CO_2 hydrogenation over Rh.[4] Thus, we studied the influence of OH- and H-groups on the properties of the catalyst and developed optimized models of surfaces with varying coverages (Figure 7d). OH groups tend to absorb on the oxyphilic FeO_x surface near the interface, while H absorbs on the alloy surface (Figure S30). We also found that the stability of methoxy groups decreases with the presence of −OH groups (Figure 7e), while H groups have the opposite effect. Interestingly, our calculations show

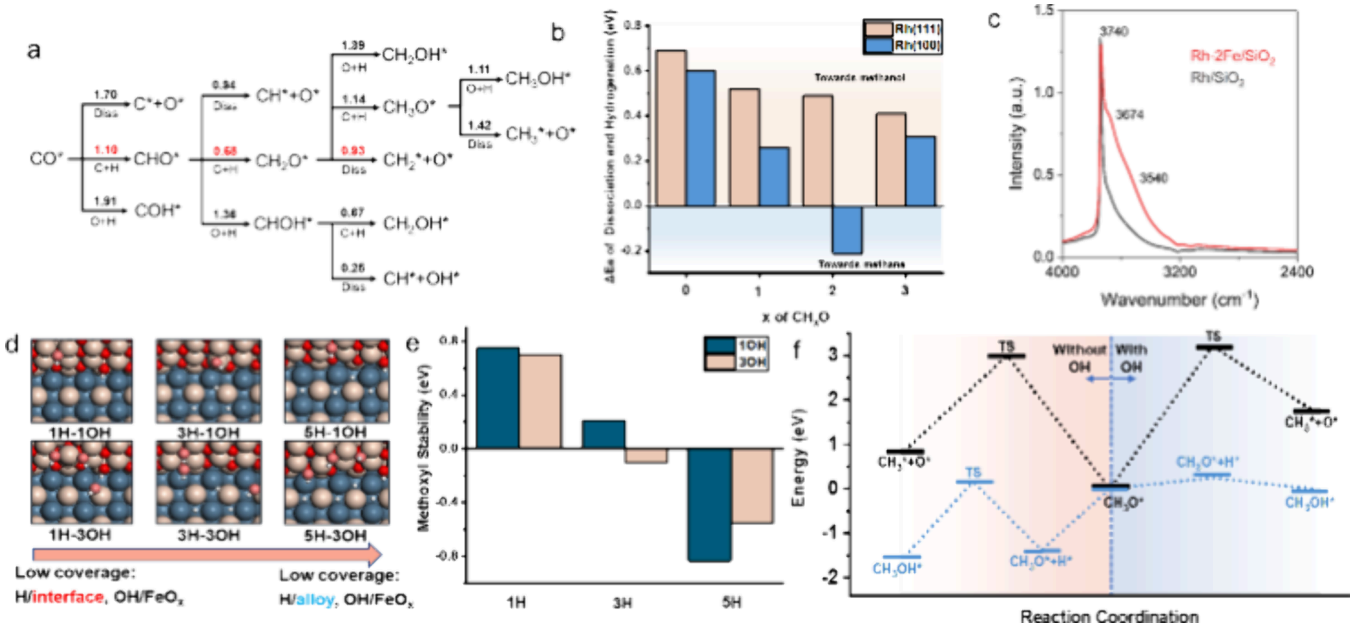

Figure 7. (a) Plausible reaction pathways for the hydrogenation of surface intermediates starting from CO* on Rh (100). (b) Difference between activation barriers of C−O dissociation and hydrogenation, where CH_2O* on Rh(100) leads to methane production on metallic Rh. (c) IR spectra of Rh−2Fe/SiO_2 and Rh/SiO_2 in 1 bar H_2 at 200 °C. The samples were reduced at 400 °C in H_2 flow, transferred into the IR chamber, and then ramped up to 200 °C in 1 bar H_2 flow. (d) Optimized OH and H adsorption structures under different coverages. Oxygen atoms of the FeO_x overlayers are shown in red, and O_2 atoms of absorbed OH are light red. (e) Methoxy stability with different coverages of coabsorbed OH and H on the interface of Rh−Fe−FeO_x. (f) Potential energy of dissociation and hydrogenation reaction of methoxy without OH and with OH.

that the hydrogen addition step that yields methanol has a barrier of 1.54 eV in the absence of adsorbed OH* groups but becomes a barrier-free process on a hydroxylated surface (Figure 7f). Hence, surface hydroxylation promotes the hydrogenation of intermediates, although the adsorption of H is weakened to 0.25 eV, which destabilizes the ground state prior to hydrogenation. In contrast, OH* groups do not influence the cleavage of the C−O bond of the methoxy group. This step keeps the barrier of around 3 eV. This high barrier indicates that the cleavage of methoxy groups hardly occurs at the interface of oxide and metal phases regardless of the presence of OH* groups. In general, these hydroxy groups influence the adsorption of species that bind at the surface through oxygen bonds but do not affect adsorbates that bind at the surface through the carbon atom.

CONCLUSIONS

We incorporated Fe species onto Rh nanoparticles to produce complex bifunctional catalysts that contain a surface alloy adjacent to Rh−O−Fe sites in nanoscopic FeO_x domains. These oxide overlayers create a "reverse catalyst"-type structure (i.e., a metal oxide supported on a metal) that increases the density of interfacial sites compared with traditional supported catalysts, where interfaces are present only at the perimeter of supported metal nanoparticles. The atomic contact between the metal nanoparticle and the oxide overlayer induces the formation of a surface Rh−Fe alloy that moderates the activity of the metal for complete C−O bond cleavage. Consequently, the multifunctional sites over FeO_x/Rh−Fe catalysts meet the following requirements of a selective catalyst for methanol formation: (1) strong interaction with CO_2 to ensure a high density of transition states, (2) metal sites to activate and make hydrogen available to surface intermediates, and (3) high energy barriers for the complete cleavage of C−O bonds to form carbides.

The FeO_x−metal interface plays a key role in the performance of the FeO_x/Rh−Fe catalysts. Sites at such interfaces interact with CO_2 much stronger than sites on Rh and Rh−Fe alloy surfaces. The energy barriers to cleave the C−O bonds of several intermediates (i.e., CH_3O* and CHOH* species) are larger on the interface than on the metal surface by at least 1 eV. Also, the interface offers a barrierless pathway for the hydrogenation of methoxy species to methanol. This property of the interface is enabled by OH* groups, which are stabilized by their spatial separation from H* (located at the metal surface).

Overall, we show how the selectivity of a metal for CO_2 hydrogenation is steered toward methanol. Our approach consists of (1) covering the whole nanoparticle with interfacial sites, which ensures high coverage of activated CO_2, and (2) changing the intrinsic activity of the underlying metal to open optimum energy pathways toward methanol. This synthetic and catalytic chemistries, demonstrated for Rh−Fe−FeO_x interfaces, enable us to overcome the limitations to the design of methanol production catalysts.

ASSOCIATED CONTENT

Supporting Information

Experimental procedures, results and discussion, survey of catalysts for methanol production from CO_2 hydrogenation, extended X-ray absorption fine structure (EXAFS) spectroscopy characterization, discussions of the Fe coordination environment and identification of the Fe−Rh alloyed species, fitting of Langmuir isotherms

to IR data of adsorbed CO, and details of the theoretical study (PDF)

AUTHOR INFORMATION

Corresponding Authors

Jinlong Gong − *School of Chemical Engineering and Technology, Collaborative Innovation Center of Chemical Science and Engineering, Tianjin University, Tianjin 300072, China*; orcid.org/0000-0001-7263-318X; Email: Gutierrez@pnnl.gov

Zhi-Jian Zhao − *School of Chemical Engineering and Technology, Collaborative Innovation Center of Chemical Science and Engineering, Tianjin University, Tianjin 300072, China*; orcid.org/0000-0002-8856-5078; Email: zjzhao@tju.edu.cn

Oliver Y. Gutiérrez − *Institute for Integrated Catalysis, Pacific Northwest National Laboratory, Richland, Washington 99354, United States*; orcid.org/0000-0001-9163-4786; Email: jlgong@tju.edu.cn

Authors

Yifeng Zhu − *Institute for Integrated Catalysis, Pacific Northwest National Laboratory, Richland, Washington 99354, United States*

Ran Luo − *School of Chemical Engineering and Technology, Collaborative Innovation Center of Chemical Science and Engineering, Tianjin University, Tianjin 300072, China*

Honghong Shi − *Institute for Integrated Catalysis, Pacific Northwest National Laboratory, Richland, Washington 99354, United States*

Katherine Koh − *Institute for Integrated Catalysis, Pacific Northwest National Laboratory, Richland, Washington 99354, United States*

Libor Kovarik − *Institute for Integrated Catalysis, Pacific Northwest National Laboratory, Richland, Washington 99354, United States*

John L. Fulton − *Institute for Integrated Catalysis, Pacific Northwest National Laboratory, Richland, Washington 99354, United States*; orcid.org/0000-0001-9361-9803

Johannes A. Lercher − *Institute for Integrated Catalysis, Pacific Northwest National Laboratory, Richland, Washington 99354, United States*

Author Contributions

∇

These authors contributed equally. The manuscript was written through contributions of all authors. All authors have given approval to the final version of the manuscript.

Funding

This work is supported by the U.S. Department of Energy (DOE), Office of Science, Office of Basic Energy Sciences, Division of Chemical Sciences, Geosciences and Biosciences (FWP 47319).

Notes

The authors declare no competing financial interest.

ACKNOWLEDGMENTS

Our research used resources of the Advanced Photon Source, a Department of Energy (DOE) Office of Science user facility operated by Argonne National Laboratory, and was supported by the DOE under contract no. DE-AC02-06CH11357 and the Canadian Light Source and its funding partners. X-ray adsorption spectra were taken with the help of Dr. Mahalingam Balasubramanian at Argonne National Laboratory.

REFERENCES

(1) Yarulina, I.; Chowdhury, A. D.; Meirer, F.; Weckhuysen, B. M.; Gascon, J. Recent trends and fundamental insights in the methanol-to-hydrocarbons process. *Nat. Catal.* **2018**, *1* (6), 398−411.

(2) Olsbye, U.; Svelle, S.; Bjørgen, M.; Beato, P.; Janssens, T. V. W.; Joensen, F.; Bordiga, S.; Lillerud, K. P. Conversion of Methanol to Hydrocarbons: How Zeolite Cavity and Pore Size Controls Product Selectivity. *Angew. Chem., Int. Ed.* **2012**, *51* (24), 5810−5831.

(3) Müller, S.; Liu, Y.; Kirchberger, F. M.; Tonigold, M.; Sanchez-Sanchez, M.; Lercher, J. A. Hydrogen Transfer Pathways during Zeolite Catalyzed Methanol Conversion to Hydrocarbons. *J. Am. Chem. Soc.* **2016**, *138* (49), 15994−16003.

(4) Kattel, S.; Liu, P.; Chen, J. G. Tuning Selectivity of CO_2 Hydrogenation Reactions at the Metal/Oxide Interface. *J. Am. Chem. Soc.* **2017**, *139* (29), 9739−9754.

(5) Lambeets, S. V.; Barroo, C.; Owczarek, S.; Jacobs, L.; Genty, E.; Gilis, N.; Kruse, N.; Visart de Bocarmé, T. Adsorption and Hydrogenation of CO_2 on Rh Nanosized Crystals: Demonstration of the Role of Interfacet Oxygen Spillover and Comparative Studies with O_2, N_2O, and CO. *J. Phys. Chem. C* **2017**, *121* (30), 16238−16249.

(6) Wang, S.-G.; Liao, X.-Y.; Cao, D.-B.; Huo, C.-F.; Li, Y.-W.; Wang, J.; Jiao, H. Factors Controlling the Interaction of CO_2 with Transition Metal Surfaces. *J. Phys. Chem. C* **2007**, *111* (45), 16934−16940.

(7) Liu, X.; Sun, L.; Deng, W.-Q. Theoretical Investigation of CO_2 Adsorption and Dissociation on Low Index Surfaces of Transition Metals. *J. Phys. Chem. C* **2018**, *122* (15), 8306−8314.

(8) Studt, F.; Sharafutdinov, I.; Abild-Pedersen, F.; Elkjaer, C. F.; Hummelshoj, J. S.; Dahl, S.; Chorkendorff, I.; Norskov, J. K. Discovery of a Ni-Ga catalyst for carbon dioxide reduction to methanol. *Nat. Chem.* **2014**, *6* (4), 320−324.

(9) Zhu, Y.; Zhang, X.; Koh, K.; Kovarik, L.; Fulton, J. L.; Rosso, K. M.; Gutierrez, O. Y. Inverse iron oxide/metal catalysts from galvanic replacement. *Nat. Commun.* **2020**, *11* (1), 3269.

(10) Matsubu, J. C.; Yang, V. N.; Christopher, P. Isolated Metal Active Site Concentration and Stability Control Catalytic CO_2 Reduction Selectivity. *J. Am. Chem. Soc.* **2015**, *137* (8), 3076−3084.

(11) Zhu, Y.; Yuk, S. F.; Zheng, J.; Nguyen, M.-T.; Lee, M.-S.; Szanyi, J.; Kovarik, L.; Zhu, Z.; Balasubramanian, M.; Glezakou, V.-A.; et al. Environment of Metal-O-Fe Bonds Enabling High Activity in CO_2 Reduction on Single Metal Atoms and on Supported Nanoparticles. *J. Am. Chem. Soc.* **2021**, *143* (14), 5540−5549.

(12) Kusama, H.; Okabe, K.; Sayama, K.; Arakawa, H. CO_2 hydrogenation to ethanol over promoted Rh/SiO_2 catalysts. *Catal. Today* **1996**, *28* (3), 261−266.

(13) Kangvansura, P.; Chew, L. M.; Saengsui, W.; Santawaja, P.; Poo-arporn, Y.; Muhler, M.; Schulz, H.; Worayingyong, A. Product distribution of CO 2 hydrogenation by K- and Mn-promoted Fe catalysts supported on N -functionalized carbon nanotubes. *Catal. Today* **2016**, *275*, 59−65.

(14) Li, C. S.; Melaet, G.; Ralston, W. T.; An, K.; Brooks, C.; Ye, Y.; Liu, Y. S.; Zhu, J.; Guo, J.; Alayoglu, S.; et al. High-performance hybrid oxide catalyst of manganese and cobalt for low-pressure methanol synthesis. *Nat. Commun.* **2015**, *6*, 6538.

(15) Yang, C.; Mu, R.; Wang, G.; Song, J.; Tian, H.; Zhao, Z.-J.; Gong, J. Hydroxyl-mediated Ethanol Selectivity of CO_2 Hydrogenation. *Chem. Sci.* **2019**, *10* (11), 3161−3167.

(16) Beck, A.; Zabilskiy, M.; Newton, M. A.; Safonova, O.; Willinger, M. G.; van Bokhoven, J. A. Following the structure of copper-zinc-alumina across the pressure gap in carbon dioxide hydrogenation. *Nat. Catal.* **2021**, *4* (6), 488−497.

(17) Larmier, K.; Liao, W. C.; Tada, S.; Lam, E.; Verel, R.; Bansode, A.; Urakawa, A.; Comas-Vives, A.; Coperet, C. CO_2-to-Methanol

Hydrogenation on Zirconia-Supported Copper Nanoparticles: Reaction Intermediates and the Role of the Metal-Support Interface. *Angew. Chem., Int. Ed.* **2017**, *56* (9), 2318−2323.
(18) Zhu, Y.; Zheng, J.; Ye, J.; Cui, Y.; Koh, K.; Kovarik, L.; Camaioni, D. M.; Fulton, J. L.; Truhlar, D. G.; Neurock, M.; et al. Copper-zirconia interfaces in UiO-66 enable selective catalytic hydrogenation of CO_2 to methanol. *Nat. Commun.* **2020**, *11* (1), 5849.
(19) Zhu, Y.; Zhang, X.; Koh, K.; Kovarik, L.; Fulton, J. L.; Rosso, K. M.; Gutiérrez, O. Y. Inverse iron oxide/metal catalysts from galvanic replacement. *Nat. Commun.* **2020**, *11* (1), 3269.
(20) Fielicke, A.; von Helden, G.; Meijer, G.; Pedersen, D. B.; Simard, B.; Rayner, D. M. Size and Charge Effects on the Binding of CO to Small Isolated Rhodium Clusters. *J. Phys. Chem. B* **2004**, *108* (38), 14591−14598.
(21) Swart, I.; de Groot, F. M. F.; Weckhuysen, B. M.; Rayner, D. M.; Meijer, G.; Fielicke, A. The Effect of Charge on CO Binding in Rhodium Carbonyls: From Bridging to Terminal CO. *J. Am. Chem. Soc.* **2008**, *130* (7), 2126−2127.
(22) Karelovic, A.; Ruiz, P. CO_2 hydrogenation at low temperature over Rh/γ-Al_2O_3 catalysts: Effect of the metal particle size on catalytic performances and reaction mechanism. *Appl. Catal. B: Environ.* **2012**, *113−114*, 237−249.
(23) Kim, J.; Ha, H.; Doh, W. H.; Ueda, K.; Mase, K.; Kondoh, H.; Mun, B. S.; Kim, H. Y.; Park, J. Y. How Rh surface breaks CO2 molecules under ambient pressure. *Nat. Commun.* **2020**, *11* (1), 5649.
(24) Wang, J.; Li, G.; Li, Z.; Tang, C.; Feng, Z.; An, H.; Liu, H.; Liu, T.; Li, C. A highly selective and stable ZnO-ZrO_2 solid solution catalyst for CO_2 hydrogenation to methanol. *Science Advances* **2017**, *3* (10), No. e1701290, DOI: 10.1126/sciadv.1701290.
(25) Kattel, S.; Yu, W.; Yang, X.; Yan, B.; Huang, Y.; Wan, W.; Liu, P.; Chen, J. G. CO_2 Hydrogenation over Oxide-Supported PtCo Catalysts: The Role of the Oxide Support in Determining the Product Selectivity. *Angew. Chem., Int. Ed.* **2016**, *55* (28), 7968−7973.
(26) Nelson, N. C.; Nguyen, M.-T.; Glezakou, V.-A.; Rousseau, R.; Szanyi, J. Carboxyl intermediate formation via an in situ-generated metastable active site during water-gas shift catalysis. *Nat. Catal.* **2019**, *2* (10), 916−924.
(27) Zhao, Z.-J.; Greeley, J. P. Identification of surface intermediates during ethylidyne formation on Pt (111) by calculation of infrared intensities and deuterium isotope shifts. *Surf. Sci.* **2015**, *640*, 112−118.
(28) Choi, Y.; Liu, P. Mechanism of ethanol synthesis from syngas on Rh (111). *J. Am. Chem. Soc.* **2009**, *131* (36), 13054−13061.